Journal of Alloys and Compounds 509 (2011) 9669–9674

Contents lists available at ScienceDirect

Journal of Alloys and Compounds

journal homepage: www.elsevier.com/locate/jallcom

Improvement of the electrochemical performance of nanosized α-MnO_2 used as cathode material for Li-batteries by Sn-doping

A.M. Hashem[a,*], A.M. Abdel-Latif[a], H.M. Abuzeid[a], H.M. Abbas[b], H. Ehrenberg[c,d], R.S. Farag[e], A. Mauger[f], C.M. Julien[g]

[a] National Research Centre, Inorganic Chemistry Department, Behoes St., Dokki, Cairo, Egypt
[b] National Research Centre, Physical Chemistry Department, Behoes St., Dokki, Cairo, Egypt
[c] Institute for Complex Materials, IFW Dresden, Helmholtzstr. 20, D-01069 Dresden, Germany
[d] Materials Science, Technische Universität Darmstadt, Petersenstr. 23, D-64287 Darmstadt, Germany
[e] Department of Chemistry, Faculty of Science, Al-Azhar University, Cairo, Egypt
[f] Université Pierre et Marie Curie, Institut de Minéralogie et Physique de la Matière Condensée (IMPMC), 4 Place Jussieu, 75005 Paris, France
[g] Université Pierre et Marie Curie, Physicochimie des Electrolytes, Colloïdes et Sciences Analytiques (PECSA), 4 Place Jussieu, 75005 Paris, France

ARTICLE INFO

Article history:
Received 16 May 2011
Received in revised form 20 July 2011
Accepted 22 July 2011
Available online 31 July 2011

Keywords:
Lithium ion batteries
Manganese dioxide
Tin doping
Cryptomelane

ABSTRACT

Sn-doped MnO_2 was prepared by hydrothermal reaction between $KMnO_4$ as oxidant, fumaric acid $C_4H_4O_4$ as reductant and $SnCl_2$ as doping agent. XRD analysis indicates the cryptomelane α-MnO_2 crystal structure for pure and doped samples. Thermal stabilization was observed for both oxides as detected from thermogravimetric analysis. SEM and TEM images show changes in the morphology of the materials from spherical-like particles for pristine P–MnO_2 to rod-like structure for Sn–MnO_2. Electrochemical properties of the electrode materials have been tested in lithium cells. Improvement in capacity retention and cycling ability is observed for doped oxide at the expense of initial capacity. After 35 cycles, the Li//Sn doped MnO_2 cell display lower capacity loss.

1. Introduction

Rechargeable lithium batteries are based on the use of intercalation compounds as electrodes in which lithium ions shuttle between the negative electrode (anode) and positive electrode (cathode) hosts. As cathode materials for lithium-ion batteries layered $LiCoO_2$, $LiNiO_2$ and $LiMn_2O_4$ have been extensively investigated world-wide [1,2]. Manganese dioxides (MDOs) have been intensively investigated as electrode for primary and secondary lithium batteries [3]. They exhibit a wide variety of structures that have been utilized in many applications. MnO_2 exists in several polymorphic modifications: α-, β-, γ-, ε-, δ-, and λ-MnO_2, in which the MnO_6 octahedra can periodically share their edges and vertices to generate a wide range of structures with different properties [4]. These complex structures depend on the preparation conditions and the presence of certain cations in the solution used for synthesis. Among the MDOs with large tunnel ($n \times m$) structure, compounds with regular lattice exist such as (2×2) hollandite, (2×3) romanechite and (3×3) todorokite that have potential applications in chemical separation, catalysis, or electrochemical devices. Due to their low cost, MDOs have been largely studied for use as positive electrode materials for Li primary batteries because their environmental merit and easy preparation [5], and more recently as electrode of hybrid supercapacitors [6].

It is commonly accepted that the some MDOs yield stabilization of their structure by large cations which reside in the tunnel of the framework; so the α-MnO_2 form refers to the hollandite or cryptomelane (2×2)-type according the presence of Ba^{2+} or K^+ cations, respectively. Most of the α-MnO_2 samples prepared by hydrothermal or chemical reaction depend on a two-step sequence of structure formation and ion exchange reaction [7–9]. Cryptomelane is a brown, greyish-white mineral of formula $K(Mn^{4+},Mn^{3+})_8O_{16}$, which crystallizes in the monoclinic system [10,11].

The primary driving force for implementation of MnO_2-based materials for battery applications is the cost. α-MnO_2 positive electrode material would be projected to cost 1% of $LiCoO_2$, the cathode material of choice in rechargeable Li-ion batteries. Essentially, properties such as cycle life and operation voltage and energy density may be drawback issues for MnO_2 materials, when compared to $LiCoO_2$ due to the potential cost difference. Safety margin

* Corresponding author at: National Research Centre, Inorganic Chemistry Department, Behoes St., Dokki, Cairo, Egypt. Tel.: +20 106305012; fax: +20 233370931.
E-mail address: ahmedh242@yahoo.com (A.M. Hashem).

0925-8388/$ – see front matter © 2011 Elsevier B.V. All rights reserved.
doi:10.1016/j.jallcom.2011.07.075

to over-charge conditions of Li-MnO_2 system, better than for Co or Ni based Li-ion batteries, is due to the stable nature of Mn(IV), which is a common oxidation state for Mn and one that retains oxygen. Manganese is also an abundant transition metal; it is the twelfth most abundant element in the earth's crust. Therefore, MnO_2 type materials are attractive for large energy storage applications, which would require very large quantities of materials to supply an emerging market [12,13].

Several works were carried out to stabilize and improve the structure of MnO_2 using counter ions such as Li^+, Na^+, Mg^{2+} [8], by doping with Al^{3+}, Co^{3+} or Ag^+ metal ions [5,14,15], with Li_2O [16]. Because the conduction mechanism in MDOs is governed by mixed valency, the ratio Mn^{4+}/Mn^{3+} redox is an important parameter. Surface modification with protective coating was also carried out with aim to enhance the cycle ability of MnO_2 as cathode in lithium batteries [17,18]. A method was proposed by Cai et al. [19] to dope transition-metal iron ions into the framework instead of the tunnels of (2×2) tunnel structure manganese octahedral molecular cryptomelane. Recently, Gulbinska and Suib [20] substituted V^{5+} for Mn^{4+} in porous MDOs producing flat discharge profiles.

In this work, we have successfully prepared nanosized particles of pure P–MnO_2 and Sn-doped MnO_2 materials via a hydrothermal redox method between $KMnO_4$ and fumaric acid. The effect of doping on the structure, morphology and electrochemical properties has been investigated. Electrochemical tests were performed in lithium cells by cyclic voltammetry and galvanostatic charge–discharge

2. Experimental

Hydrothermal redox reaction between potassium permanganate ($KMnO_4$) as the oxidizing agent and fumaric acid ($C_4H_4O_4$) as reducing agent was used to prepare nanosized pure MnO_2 (P–MnO_2) and Sn-doped MnO_2 (Sn–MnO_2). Molar ratio of 3:1 of $KMnO_4$:$C_4H_4O_4$ was used to prepare P–MnO_2. 3:1:0.07 $KMnO_4$:$C_4H_4O_4$:$SnCl_2$ molar ratio was used for Sn–MnO_2. This molar ratio between oxidizing and reducing agents allows the effective oxidation state of the Mn in the final product to be around Mn^{4+}. After one hour of stirring in slight acidic solution, dark brown precipitate was formed at room temperature. The formation of MnO_2 was the result of the oxidation of fumaric acid into volatile CO_2 and soluble $H_2C_2O_4$, while $[MnO_4]^-$ ions were reduced to MnO_2 leading to total consumption of the reactants. Complete reduction of $KMnO_4$ can be observed also from a change in color of the supernatant liquid from purple to dark brown. The formed precipitate was collected by filtration. To allow the removal of K^+ from the precipitate we washed it several times with distilled water. The resulting precipitate was dried at 100 °C for 24 h producing a black powder after calcination the dried powder in an ambient atmosphere at 450 °C for 6 h.

The crystalline phase was identified by X-ray diffraction (XRD) using Philips X'Pert PROMRO (PW3050) apparatus equipped with a CuK_α X-ray anticathode ($\lambda = 1.5406$ Å). XRD measurements were collected under Bragg–Brentano geometry in the 2θ range 10–80° with step of 0.05°. TG measurements were carried out using a thermal gravimetric analyzer (Perkin Elmer, TGA 7 series) in the temperature range of 30–1000 °C in air at a heating rate of 10 °C/min. The particle morphology of the MnO_2 powders was investigated by scanning electron microscope (SEM, JEOL-Japan, JXA-840A) and by transmission electron microscope (TEM, JEOL-1230).

The electrochemical tests were performed using a multichannel potentiostatic–galvanostatic system VMP (Perkin Elmer Instruments, USA). The cathode mixture for the fabrication of the positive electrode was prepared by mixing 80 wt.% of the active material with 10 wt.% of super P® Li carbon (TIMCAL) and 10 wt.% of polyvinylidene fluoride binder (PVDF), dissolved in N-methyl pyrrolidone (NMP). For the electrochemical studies, about 10 mg of this mixture was pressed at a pressure of 5 tons on an aluminum mesh and dried at 100 °C for 1 h in a vacuum oven. Swagelok-type cells were assembled in an argon filled dry box with Li-foil as anode and glass–fiber separator soaked with 1 mol L^{-1} $LiPF_6$ in EC–DMC (1:2) as organic electrolyte. Galvanostatic charge–discharge cycling was carried out at C/15 rate in the voltage range 1.5–4.0 V vs. Li/Li^+.

3. Results and discussion

3.1. Structure and morphology

Fig. 1 shows the XRD patterns of P–MnO_2 (a) and Sn–MnO_2 (b) samples. The diagram of pure α-MnO_2 is composed of rather

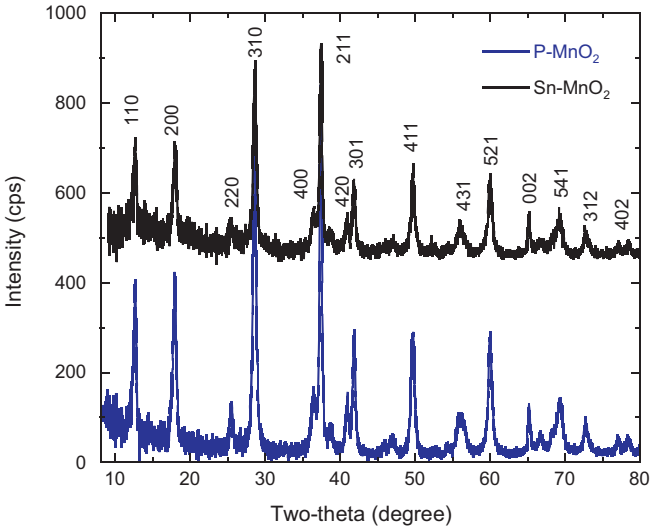

Fig. 1. XRD of (a) P–MnO_2 and (b) Sn–MnO_2. Samples were synthesized through redox reaction between $KMnO_4$ and fumaric acid $C_4H_4O_4$. Doped compound was prepared using $SnCl_2$.

broad diffraction peaks. All these peaks are indexed to a pure cryptomelane α-MnO_2 with the tetragonal phase (I4/*m* space group) in agreement with the JCPDS file #44-0141. As shown in the XRD diagram of the Sn–MnO_2 sample, the doping does not have any significant effect on the crystal structure of manganese dioxide. All the *h k l* reflections were labeled along with the Miller indices of the α-MnO_2 phase. No extra peaks related to Sn impurities were observed. The absence of modification in the XRD diagrams might indicate that: (i) Sn is in low content or has crystalline domains beyond the detection limit of XRD; (ii) Sn is incorporated in the cryptomelane structure, with the formation of a solid solution; and/or (iii) Sn is incorporated into the channels of cryptomelane structure, replacing K^+ ions in the (2×2) tunnels.

The lattice parameters *a* and *c* of the tetragonal structure for the MDOs synthesized materials were calculated by the least-squares refinement method using 12 well-defined XRD lines. Data are listed in Table 1. Attempt to make Rietveld refinement was unsuccessful because the low X-ray scattering efficiency that makes to poor signal recorded. It appeared very often in the case of MnO_2 as mentioned by Pannetier and Chabre [4]. It is observed that no significant change occurs in lattice parameters, thus the cryptomelane structure is preserved upon tin doping. Notice that the success of tin doping in MnO_6 octahedra is due to the similarity in the ionic radii of octahedral high-spin Mn^{3+} (0.65 Å) and Sn^{4+} (0.69 Å) in crystal. Thus, Sn^{4+} can substitute for Mn^{3+} without causing much structural disorder and serious charge imbalance. Cai et al. have shown that incorporation of iron in the tunnel structure cryptomelane did not change the charge of the framework [19]. We have carried out magnetic measurements to verify the Sn^{4+} substitution. Results show a decrease of the magnetic moment upon Sn doping, from 4.23 to 3.9 μ_B that indicates the decrease of Mn^{3+} concentration in the MnO_2 lattice.

Table 1
Lattice parameters of P–MnO_2 and Sn–MnO_2 samples.

Sample	Lattice parameters		
	a (Å)	*c* (Å)	*V* (Å^3)
P–MnO_2	9.85(6)	2.86(1)	277.9
Sn–MnO_2	9.86(1)	2.86(1)	278.239

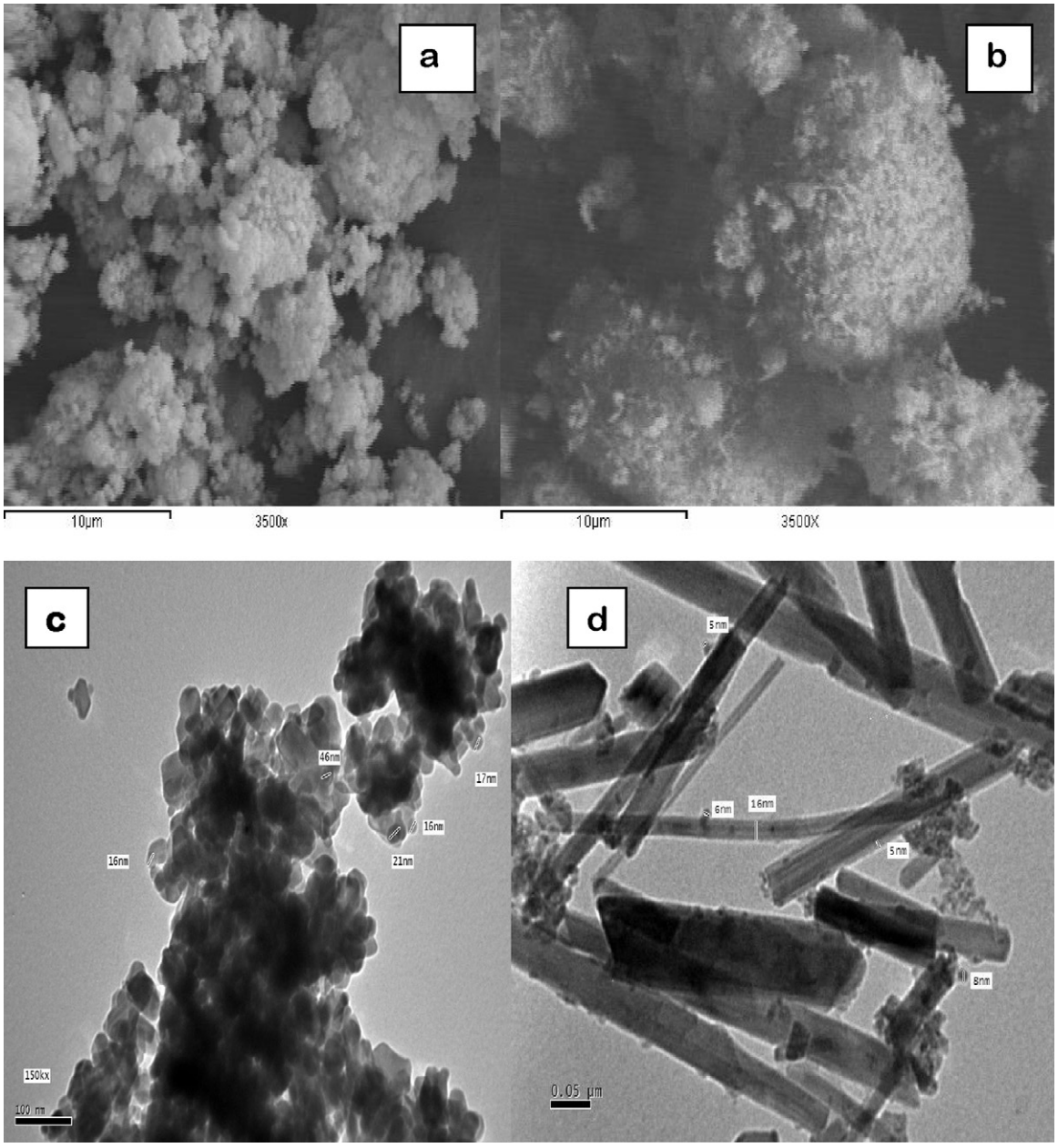

Fig. 2. SEM and TEM images of (a and c) P–MnO_2 and (b and d) Sn:MnO_2 oxides, respectively.

The relatively broad diffraction peaks of the XRD patterns indicate small particle size for MDOs powders. The coherence length, L_c, has been estimated using Scherrer formula

$$L_c = \frac{K\lambda}{\beta \cos\theta} \quad (1)$$

where β is the full width at half maximum (FWHM) in radians, the constant is $K = 0.9$, λ is the wavelength of the X-ray, θ is the corresponding Bragg angle. We find $L_c = 18 \pm 0.5$ nm that corresponds to the particle size, L, estimated from the SEM images (see below).

Fig. 2a and b represents the SEM images of P–MnO_2 and Sn–MnO_2 samples. With the magnification used for the SEM investigations, the two samples have similar non-uniform spongy-like structure showing very small particles, $L < 100$ nm. It is shown that particles have the tendency to agglomerates. The TEM images of the same samples show difference in the morphology (Fig. 4c and d). A big difference in the shape of particles is observed. Spherical-like particles with size ca. 30 nm were observed for P–MnO_2, while Sn doped MnO_2 powders display a rod-like morphology with particles 15 nm thick and 200 nm length. Note that the diameters of these nanorods observed by SEM are very close to the particle size calculated by Eq. (1). Obviously, these results show that the Sn doping alters the shape of the particles. This could be attributed to the replacement of Sn^{4+} for Mn^{3+} and the increasing amount of K^+ ions in the (2×2) tunnels. It has been pointed out by several workers that the particle morphology is strongly dependent on the synthetic conditions. For instance, the direct reaction of potassium permanganate with fumaric acid via a mild hydrothermal route favors the growth of α-MnO_2 nanowires or nanorods [21–24]. Portehault et al. have shown that the monocrystalline primary nanorods are well ordered together at low pH on the mesocrystal [23].

3.2. Thermal stability

The thermal behaviors of P–MnO_2 and Sn–MnO_2 are viewed in Fig. 3 by the thermogravimetric curves recorded in the tem-

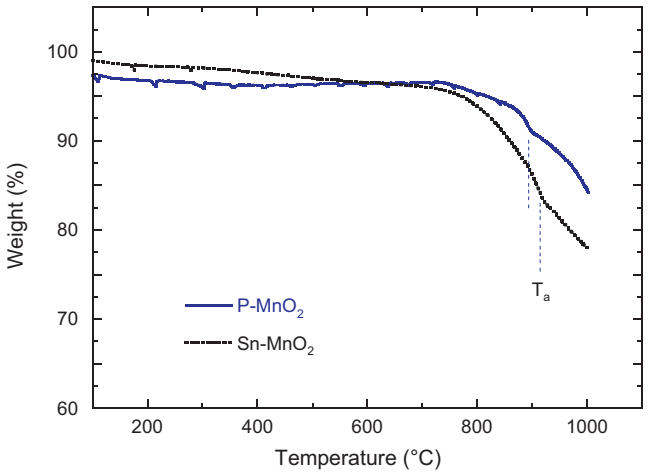

Fig. 3. Curves of the thermogravimetric analysis for P–MnO_2 and the Sn–MnO_2 oxides.

perature range 30–1000 °C in air at 10 °C/min heating rate. There is almost no difference in the thermal behaviors of both oxides excepted a small change in the vicinity of 900 °C. Both oxides showed thermal stabilization due to high percent of K^+ ions detected by chemical analysis. A quantity of about 7 wt.% K^+ ions was evaluated in both samples. Thus the crystal chemistry of our samples synthesized via hydrothermal route is $K_{0.07}MnO_2$. The conversion of MnO_2 to Mn_2O_3 starts at ca. 700 °C in both oxides, while further thermal decomposition of Mn_2O_3 to Mn_3O_4 expected to occur above 1000 °C (out of the range of our measurements).

It could be remarked that the thermal decomposition reactions of MnO_2 containing very low content of K^+ ions occurred in two steps as reported in [29]. The first decomposition of MnO_2 to Mn_2O_3 occurs at the range of 500–600 °C. The second decomposition of Mn_2O_3 to Mn_3O_4 occurred in the range of 900–1000 °C. In this study, the decomposition to Mn_2O_3 starts at above 770 °C that means a relatively high concentration of potassium ions which functions as structural stabilization. Finally, as shown in Fig. 3, the same function occurs with a removal of Mn^{3+} by Sn^{4+} ions.

3.3. Electrochemical tests

Electrochemical properties have been investigated in Li cell with 1 mol L^{-1} $LiPF_6$ in EC–DMC (1:2) as organic electrolyte. Fig. 4a and b show the cyclic voltammograms of P–MnO_2 and Sn–MnO_2, respectively. The reduction peaks (discharge process) are observed at ca. 2.25 and 2.20 V for P–MnO_2 and Sn–MnO_2, respectively. In both samples the reduction peak occurring at the first discharge is shifted to higher potentials in the second and forthcoming cycles. The change in peak position upon cycling has been attributed to a structural evolution in γ-MnO_2 [25]. The marked change of the reduction voltammogram from first to second reduction is still observed as in other MDOs. It has been attributed to the reduction of surface states mainly in view of its high kinetic reversibility [4]. Brown and Altermatt have shown that a monolayer of water at the surface of γ-MnO_2 is responsible for the peak at ca. 0.1 V vs. Hg/HgO [26].

The discharge–charge profile of Li//Manganese dioxide cells for both P–MnO_2 and Sn–MnO_2 are shown in Fig. 5a and b. It is obvious that the cell with Sn doped MnO_2 displays better rechargeability than cell built with P–MnO_2 as positive electrode; the latter exhibits higher capacity fading.

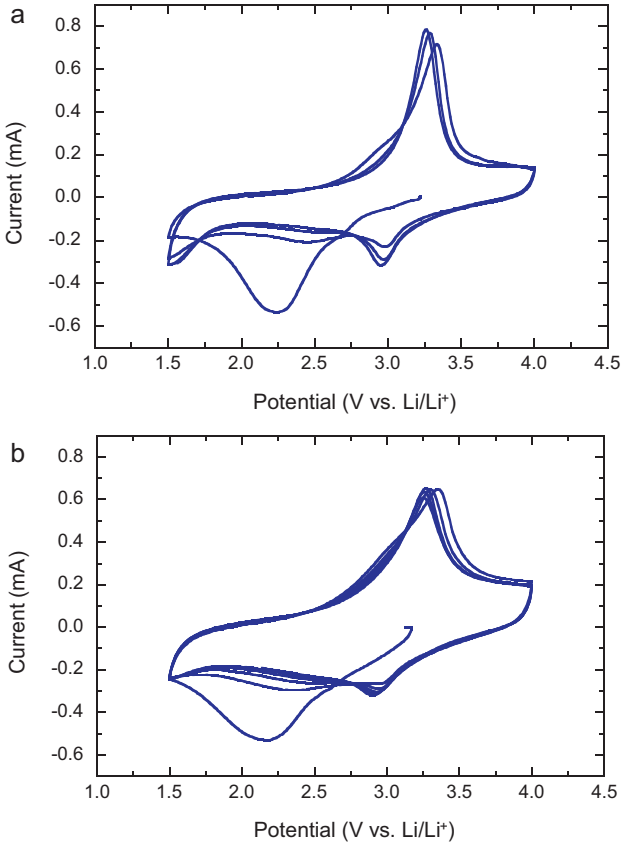

Fig. 4. Cyclic voltamograms of (a) P–MnO_2 and (b) Sn–MnO_2 using a scan rate 0.05 V/s in the voltage range 1.5–4.0 V vs. Li/Li^+.

In the case of stoichiometric MnO_2 all Mn^{4+} cations can be reduced to Mn^{3+} giving a theoretical gravimetric capacity 308 mAh/g. The cell with P–MnO_2 delivers a discharge capacity of 160 mAh g^{-1} at the first cycle. It seems that the presence of large bulky cations, e.g. K^+, impede the easy diffusion of Li^+ ions in the tunnels of the α-MnO_2 framework. At the first order, the number of available sites for foreign ions inserted into the host and the number of available electronic states are the limiting factors for discharge capacity. The cell with Sn-doped cryptomelane delivers 120 mAh/g at the first cycle. The lower capacity could be due to the lower fraction of non electroactive Sn^{4+} ions. The lower initial capacity observed in case of Sn–MnO_2 could have several origins: (i) the presence of K^+ cations, which block the ionic motion via the large 2×2 channel in the cryptomelane structure, (ii) the replacement of Sn for Mn ions, which impede the electronic conduction and (iii) the grain morphology of α-MnO_2 electrodes, which plays an important role in the electrochemical behavior of Li//α-MnO_2 rechargeable cells. Shao-Horn et al. [27] have demonstrated that crystals with a small aspect ratio have a large electrochemically active surface because the large exposed (2×2) tunnel cross-sectional area per unit volume available for lithium insertion.

The discharge capacities vs. the cycle number for P–MnO_2 and Sn–MnO_2 are displayed in Fig. 6. The capacities at the 40th cycle are about 65 and 80 mAh/g for the P–MnO_2 and Sn–MnO_2 samples, respectively. Sn doped MnO_2 oxide retained about 71%, while P–MnO_2 retained only 40.2% from their initial capacities at 40th cycle. The fading capacity of the Li//P–MnO_2 cell is much higher than that observed in Li//Sn–MnO_2 cell. Better capacity retention and rechargeability was observed for Sn–MnO_2 at the expanse of its initial capacity. So, we can conclude that the doping process has a good impact on the electrochemical performance.

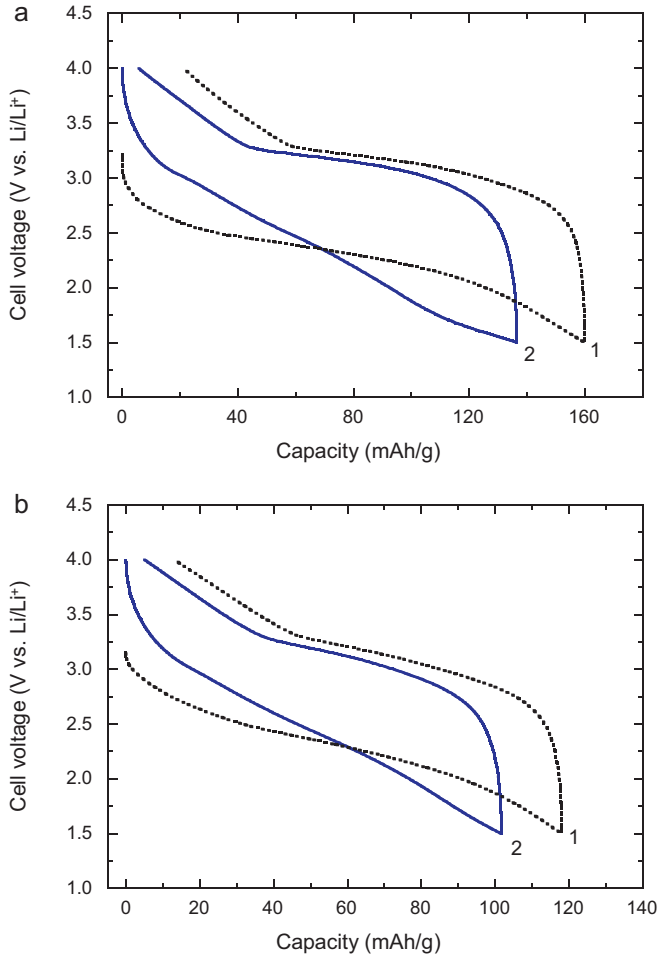

Fig. 5. Galvanostatic discharge/charge of (a) P–MnO_2 and (b) Sn–MnO_2. Data were recorded at C/15 rate in the voltage range 1.5–4.0 V vs. Li/Li^+.

The capacity loss observed in the first cycles in P–MnO_2 is attributed to the small amount of lithium ions inserted in the MnO_2 electrode and cannot be easily removed from the structure. Similar effect, but with smaller amplitude, occurs for Li//Sn–MnO_2. In spite of this drawback, presence of tin results in an enhancement of the structural stability, which can be attributed to the reduction

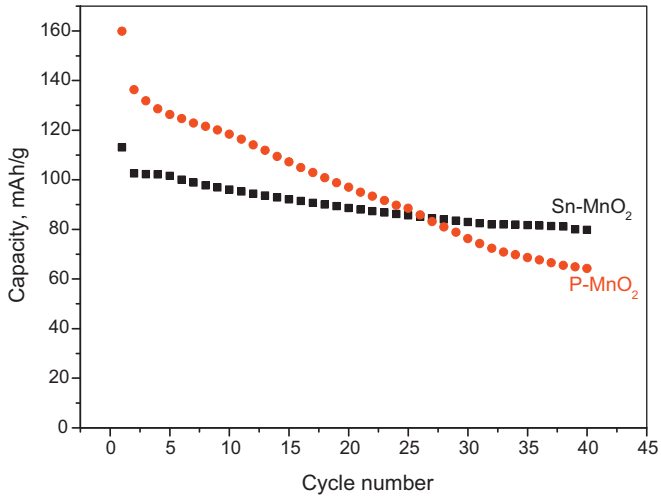

Fig. 6. Discharge capacity vs. cycle number of P–MnO_2 and Sn–MnO_2 at C/15 rate in the voltage range 1.5–4.0 V vs. Li/Li^+.

of Mn^{3+} Jahn-Teller ions. Note that the stabilization of the MnO_2 (2×2) tunnel framework has been pointed out by the Thackeray's group [27], who observe a structural instability to chemical lithiation of α-MnO_2. Also, the capacity loss in the first cycle is in most cases due to the shaping of the electrode. It seems that it occurred in our studies. The porosity plays an important role for the ion transfer at the interface.

The second reason for this degradation in the capacity in P–MnO_2 upon cycling may be related to significant amount of Mn^{2+} ions formed at the end of the discharge. The Mn^{2+} ions can be dissolved into the electrolyte causes significant increase in the capacity fading of lithium manganese oxides [15,28]. It seems that these two drawbacks were alleviated after doping by Sn. However, we got better capacity retention and better recharge ability for Sn–MnO_2 in comparison with P–MnO_2. This remarkable improvement in electrochemical behavior observed for Sn–MnO_2 is attributed to stabilization in the structure and/or enhancement of electrical conductivity after doping with Sn. In previous work [14], we reported that doping MnO_2 with Sn improves both the structure stability and electrical conductivity of α-MnO_2. Thermal stabilization and good electrical conductivity have positive effects on the behavior of α-MnO_2 in alkaline batteries [14]. The same effect was observed here in this study in the case of lithium battery.

4. Conclusion

In this work, nanosized manganese dioxide and its tin-doped product have been prepared by wet-chemical method. XRD analysis confirmed the cryptomelane-like structure of MnO_2 and showed that no extra peaks related to tin metal or impurities were observed for MnO_2 oxides after doping. The net effect of Sn doping observed from TEM images is a change in the morphology of MnO_2 particles that exhibit a nanorod-like shape. Doping MnO_2 by Sn improved the capacity retention and the rechargeability of MnO_2 at the expanse of the initial capacity.

Acknowledgments

Financial support from the Deutsche Forschungsgemeinschaft (DFG) within the Research Collaborative Centre 595 on "Electrical Fatigue in Functional Materials" is gratefully acknowledged.

References

[1] W. Kim, K. Chung, Y. Choi, Y. Sung, J. Power Sources 115 (2003) 10.
[2] W. Dreyer, J. Jamnik, C. Guhlke, R. Huth, J. Moškon, M. Gaberšcek, Nat. Mater. 9 (2010) 448.
[3] Y.F. Shen, R.P. Zerger, R.N. Guzman, S.L. Suib, L. McCurdy, L.I. Potter, C.L. O'Young, Science 260 (1993) 511.
[4] Y. Chabre, J. Pannetier, Prog. Solid State Chem. 23 (1995) 1.
[5] E. Machefaux, A. Verbaere, D. Guyomard, J. Power Sources 157 (2006) 443.
[6] T. Brousse, P.-L. Taberna, O. Crosnier, R. Dugas, P. Guillemet, Y. Scudeller, Y. Zhou, F. Favier, D. Belanger, P. Simon, J. Power Sources 173 (2007) 633.
[7] G.V. Sokol'skii, S.V. Ivanov, N.D. Ivanova, E.I. Boldirev, J. Electrochem, Powder Metall. Met. Ceram. 45 (2006) 3.
[8] M.Y. Liao, J.M. Lin, J.H. Wang, C.T. Yang, T.L. Chou, B.H. Mok, N.S. Chong, H.Y. Tang, Electrochem. Commun. 5 (2003) 312.
[9] C.S. Johnson, J. Power Sources 165 (2007) 559.
[10] S.L. Suib, Curr. Opin, Solid State Mater. Sci. 3 (1998) 63.
[11] S. Ching, J.L. Roark, N. Duan, S.L. Suib, Chem. Mater. 9 (1997) 750.
[12] H. Malankar, S.S. Umare, K. Singh, J. Mater. Lett. 63 (2009) 2016.
[13] Y. Lu, L. Yang, M. Wei, Y. Xie, T. Liu, J. Solid State Electrochem. 11 (2007) 11.
[14] A.M.A. Hashem, H.A. Mohamed, A. Bahloul, A.E. Eid, C.M. Julien, Ionics 14 (2008) 7.
[15] H.M. Abuzeid, A.M. Hashem, N. Narayanan, H. Ehrenberg, C.M. Julien, Solid State Ionics 182 (2011) 108.
[16] C.S. Johnson, D.W. Dees, M.F. Mansuetto, M.M. Thackeray, D.R. Vissers, D. Argyriou, C.-K. Loong, L. Christiensen, J. Power Sources 68 (1997) 570.
[17] R. Liu, S.B. Lee, J. Am. Chem. Soc. 130 (2008) 2942.
[18] A. Bahloul, B. Nessark, F. Habelhames, C.M. Julien, Ionics 17 (2011) 239.
[19] J. Cai, J. Liu, W.S. Willis, S.L. Suib, Chem. Mater. 13 (2001) 2413.
[20] M.K. Gulbinska, S.L. Suib, J. Power Sources 196 (2011) 2149.

[21] Y. Liu, M. Zhang, J. Zhang, Y. Qian, J. Solid State Chem. 179 (2006) 1757.
[22] L. Li, Y. Pan, L. Chen, G. Li, J. Solid State Chem. 180 (2007) 2896.
[23] D. Portehault, S. Cassaignon, E. Baudrin, J.P. Jolivet, Chem. Mater. 19 (2007) 5410.
[24] Y. Khan, S.K. Durrani, M. Mehmood, M.R. Khan, J. Mater. Sci. (2011), doi:10.1557/jmr.2011.138.
[25] L.I. Hill, A. Verbaere, D. Guyomard, J. Power Sources 119–121 (2003) 226.
[26] I.D. Brown, D. Altermatt, Acta Cryst. B 41 (1985) 244.
[27] Y. Shao-Horn, S.A. Hackney, C.S. Johnson, M.M. Thacheray, J. Electrochem. Soc. 145 (1998) 582.
[28] D.H. Jang, Y.J. Shin, S.M. Oh, J. Electrochem. Soc. 143 (1998) 2204.
[29] T. Ohzuku, I. Tari, T. Hirai, J. Electrochim. Acta 27 (1982) 1049.